Optical Nonlinearity in Cu_2CdSnS_4 and α/β-Cu_2ZnSiS_4, Diamond-like Semiconductors with High Laser-Damage Thresholds

Kimberly A. Rosmus,[a] Jacilynn A. Brant,[a] Stephen D. Wisneski,[a] Daniel J. Clark,[b] Yong Soo Kim,[b,c] Joon I. Jang,[b] Carl D. Brunetta,[a] Jian-Han Zhang,[a] Matthew N. Srnec,[a] and Jennifer A. Aitken[a*]

[a]Department of Chemistry and Biochemistry, Duquesne University, Pittsburgh, PA 15282, USA
[b]Department of Physics, Applied Physics and Astronomy, Binghamton University, P.O. Box 6000, Binghamton, NY 13902, USA
[c]Department of Physics and Energy Harvest-Storage Research Center, University of Ulsan, Ulsan, 680-749, South Korea

ASSOCIATED CONTENT

Supporting Information

1. Experimental

1.1 Reagents

Copper powder, 99.999%, Strem, Newburyport, MA; cadmium powder, 99.999%, Strem Newburyport, MA; silicon powder, 99.999%, Strem, Newburyport, MA; sulfur powder, sublimed, 99.5%, Fisher Scientific, Pittsburgh, PA; tin powder, 99.999%, Strem, Newbutyport, MA; zinc powder, 99.999%, Strem, Newburyport, MA.

1.2 Synthesis

Cu_2CdSnS_4 and α/β-Cu_2ZnSiS_4 were prepared via high-temperature solid-state synthesis. The starting materials were weighed in stoichiometric amounts, where 1 mmol was used as 1 equivalent, and ground in an agate mortar and pestle for 30 min in an argon-filled glove box. Each sample was placed into a graphite crucible, which was then inserted into a 12 mm outer diameter fused-silica tube. The tube was flamed-sealed under a vacuum of 10^{-3} mbar using an oxy-methane torch. The samples of Cu_2CdSnS_4 were heated to 800 °C over 12 h and held at that temperature for 125 h. The samples were then cooled to 500 °C over 50 h, at a rate of 6 °C/hr and then cooled to ambient temperature. The heating profile for α/β-Cu_2ZnSiS_4 can be found in Rosmus et al.[1]

1.3 Single Crystal X-ray Diffraction

A Bruker SMART Apex II CCD single crystal X-ray diffractometer employing graphite monochromatized molybdenum K_α radiation with a wavelength of 0.71073 Å and operating with a tube power of 50 kV and 30 mA was used to collect the data for 40 s/frame at ambient temperature. A total of 2930 measured reflections was collected with 293 of them unique. The program SAINT[2] was used to integrate the data and SADABS[3] was employed to perform the absorption correction. XPREP was used for space group determination and to create files for SHELXTL. Based on systematic absences, I-*4* (#82), I*4*/*m* (#87), I*4* (#79), I-*42m* (#121), I*4*/*mmm* (#139), I-*4m2* (#119), I*422* (#97) and I*4mm* (#107) were suggested space groups for Cu_2CdSnS_4. Because diamond structures are inherently noncentrosymmetric and there exist diamond-like materials crystallizing in I-*4* and I-*42m,* these space groups were further considered. Since the data clearly showed systematic absences for hkl: l=2n, the space group I-*42m* was selected. The structure was solved using direct methods. Four atoms were located in special positions. Results can be found in Table S1 and the deposited crystallographic information file (cif).

Table S1. Results from single crystal X-ray diffraction data for Cu_2CdSnS_4.

Space group	I-*42m (No.121)*
Crystal size	0.06 mm x 0.05 mm x 0.03 mm
Formula weight	486.41 g mol^{-1}
Temperature	293(2) K
Unit cell dimensions	a = 5.592 (1) Å
	b = 5.592 (1) Å
	c = 10.840 (2) Å
Volume	338.969 (1) $Å^3$
Z	2
Calculated density	4.766 Mg/m^3
Reflections collected/unique	2930/293
Data/Restraints/Parameters	293/0/14
Completeness to θ=27.51	100%
Flack parameter	0.04(3)
F(000)	440
Final R indices [I > 2σ(I)]	R1=0.0090, wR2=0.0196
Final R indices (all data)	R1=0.0086, wR2=0.0193
Goodness of fit	1.16
Largest peak	0.90 $e^- Å^{-3}$
Deepest hole	-0.368 $e^- Å^{-3}$
Refinement of F^2 was made against all reflections. $R_1 = (\Sigma \| \|F_o\| - \|F_c\| \|)/(\Sigma \|F_o\|)$, $wR_2 = \sqrt{(\Sigma[w(F_o^2-F_c^2)^2]/\Sigma[w(F_o^2)^2])}$, $w = 1/[\sigma^2(F_o^2) + (aF_o)^2 + bP]$, $P = [2F_c^2 + Max(F_o^2,0)]/3$	

1.4 High-Resolution Synchrotron X-ray Powder Diffraction

High-resolution synchrotron powder diffraction data were collected using beamline 11-BM at the Advanced Photon Source (APS), Argonne National Laboratory using an average wavelength of 0.413838 Å for powdered samples of α/β-Cu_2ZnSiS_4 as well as Cu_2CdSnS_4, which was ground with silicon standard. Discrete detectors covering an angular range from -6 to 16° 2θ were scanned over a 34° 2θ range, with data points collected every 0.001° 2θ and a scan speed of 0.01°/s. The 11-BM instrument uses X-ray optics with two platinum-stripped mirrors and a double-crystal Si(111) monochromator, where the second crystal has an adjustable sagittal bend.[4] Ion chambers monitor incident flux. A vertical Huber 480 goniometer, equipped with a Heidenhain encoder, positions an analyzer system comprised of twelve perfect Si(111) analyzers and twelve Oxford-Danfysik $LaCl_3$ scintillators, with a spacing of 2° 2θ.[5] The sample was spun during data collection. A Mitsubishi robotic arm was used to mount and dismount the sample on the diffractometer.[6] Data were collected at room temperature.

The diffractometer was controlled via EPICS[7] and data were collected while continually scanning the diffractometer 2θ arm. A mixture of NIST standard reference materials, Si (SRM 640c) and Al_2O_3 (SRM 676) was used to calibrate the instrument, where the Si lattice constant determines the wavelength for each detector. Corrections were applied for detector sensitivity, 2θ offset, small differences in wavelength between detectors, and the source intensity, as noted by the ion chamber before merging the data into a single set of intensities evenly spaced in 2θ. Rietveld refinements were carried out with GSAS/EXPGUI.[6,8]

The single crystal structure determined in this work was used as the starting model for Cu_2CdSnS_4. There was one peak of very low intensity that could not be identified. This peak was not even discernable via laboratory X-ray powder diffraction. Final statistics were excellent even while not accounting for this peak due to its extremely weak intensity. The background was fitted with a shifted Chebyschev polynomial with 18 terms.[9] The peak shapes were accounted for through refinement of the Lorentzian

terms within the type-3 profile. Lattice parameters, atomic coordinates, and isotropic displacement parameters were refined. The least squares for this refinement converged with χ^2 = 1.882, R_p = 0.1129 (all data) and R_{wp} = 0.1331 (all data), Figure S1.

The starting models for α-Cu_2ZnSiS_4 and β-Cu_2ZnSiS_4 were obtained from our previous work.[1,10] Additionally, ZnS was added to the starting model to account for a small impurity.[11] Moreover, there were several very weak peaks, only observable by synchrotron diffraction, that were unable to be identified. Because they were so weak, not accounting for them had little effect on the overall statistics, which were deemed excellent. The background was fitted with a shifted Chebyschev polynomial with 18 terms.9 The peak shapes were accounted for through refinement of the Lorentzian terms within the type-3 profile. Lattice parameters, atomic coordinates, and isotropic displacement parameters were refined. The weight fractions for α-Cu_2ZnSiS_4, β-Cu_2ZnSiS_4, ZnS were found to be 59(1)%, 40(1)%, and 0.3(1)%, respectively. The final refinement converged with χ^2 = 2.216, R_p = 0.0807 (all data) and R_{wp} = 0.0975 (all data), Figure S1.

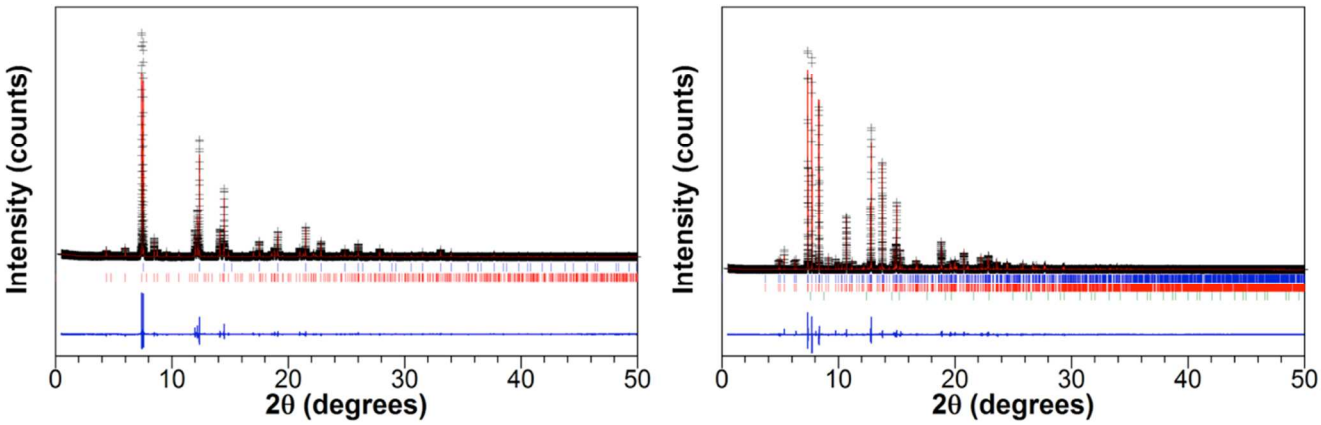

Figure S1. The Rietveld refinement results of Cu_2CdSnS_4 (left) and α/β-Cu_2ZnSiS_4 (right) using high-resolution synchrotron powder diffraction data. In each plot, the observed data (+) and the calculated data (red solid line) are shown at the top. Below the data for Cu_2CdSnS_4 are two rows of tick marks (|) corresponding to the locations of the expected Bragg reflections of Si and Cu_2CdSnS_4, from top to bottom. Below the data for α/β-Cu_2ZnSiS_4 are three rows of tick marks (|) corresponding to the locations of the expected Bragg reflections for α-Cu_2ZnSiS_4, β-Cu_2ZnSiS_4, and ZnS, from top to bottom. The difference between the observed and the calculated patterns (blue solid line) is shown at the bottom of each plot.

1.5 Scanning Electron Microscopy coupled with Energy Dispersive Spectroscopy (SEM/EDS)

Semi-quantitative elemental analysis for Cu_2CdSnS_4 and α/β-Cu_2ZnSiS_4 (Figure S2) was executed using a Hitachi S-3400N scanning electron microscope equipped with a Bruker Quantax model 400 energy dispersive spectrometer using an XFlash® 5010 EDS detector with a 129 eV resolution. Small crystals of Cu_2CdSiS_4 and α/β-Cu_2ZnSiS_4 were attached to double-sided carbon tape that was adhered onto an aluminum specimen holder. EDS spectra were collected for three areas on each of three crystals for both specimens at an accelerating voltage of 15 kV for 5 min live time at a working distance of 10 mm.

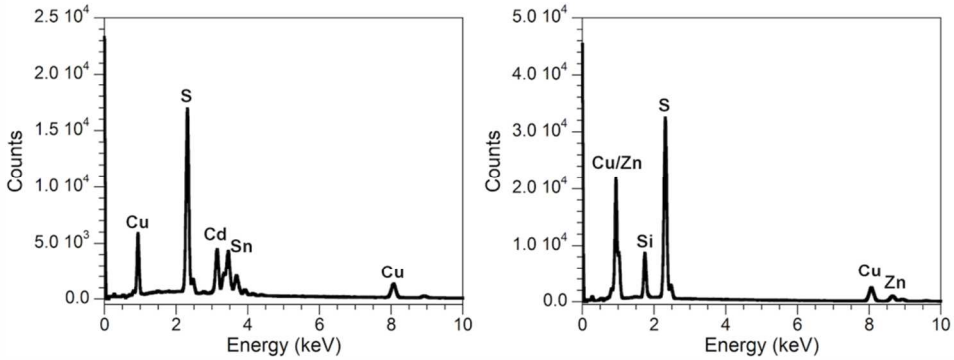

Figure S2. Representative EDS spectra of Cu_2CdSnS_4 (left) and α/β-Cu_2ZnSiS_4 (right).

When determining the composition of each compound, the oxygen and carbon from the carbon tape and the aluminum from the specimen holder were subtracted to acquire a composition based only on the elements within the crystals. The compositions were found to be $Cu_{2.2}Cd_{1.0}Sn_{1.0}S_{3.9}$ and $Cu_{2.1}Zn_{1.0}Si_{0.9}S_{3.5}$, which are close to the nominal compositions.

1.6 Differential Thermal Analysis (DTA)

A Shimadzu DTA-50 thermal analyzer was employed for thermal analysis studies of Cu_2CdSnS_4 and α/β-Cu_2ZnSiS_4. A three-point calibration curve using the melting points of indium, zinc and gold metals was used to calibrate the instrument. The samples and an Al_2O_3 reference material of similar mass were sealed under vacuum in carbon-coated, fused-silica ampoules. The temperature was programmed to increase at a rate of 10 °C/min to 1000 °C, held for 1 min, and then cooled at 10 °C/min. Two cycles were performed in order to distinguish reversible and irreversible events (Figure S3).

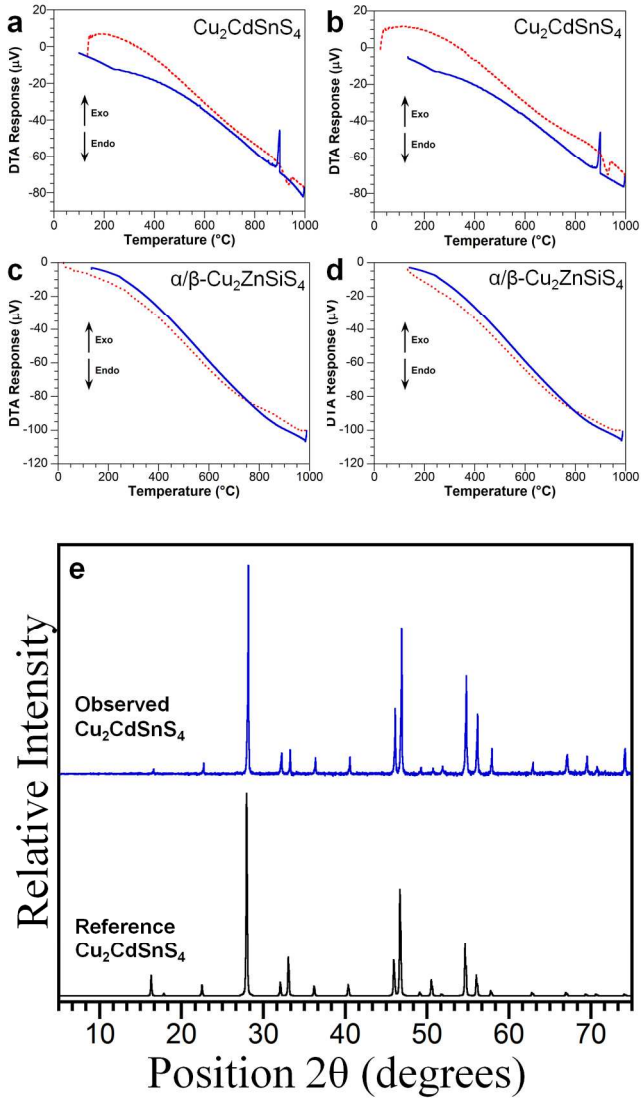

Figure S3. Differential thermal analysis diagrams of the first heating/cooling cycle for (a) Cu_2CdSnS_4 and (c) α/β-Cu2ZnSiS4. The second cycle for (b) Cu_2CdSnS_4 and (d) α/β-Cu_2ZnSiS_4. The heating cycles are shown by the red dashed curves and the cooling cycles are depicted as blue solid curves. (e) Observed and calculated XRPD patterns for the DTA residue for Cu_2CdSnS_4.

The Cu_2CdSnS_4 sample exhibited one reversible event during heating and one during cooling. Each heating cycle showed an endothermic event at approximately 930°C that can be attributed to the melting point of the product, which is consistent with the melting point (926 °C) found by Matsushita et al.[12] Each cooling cycle demonstrated an exothermic event, which is due to the recrystallization of the material at approximately 900°C. The DTA diagram of α/β-Cu_2ZnSiS_4 indicates no thermal events during the heating or the cooling cycles. This suggests that the melting point of the material is greater than 1000°C. Multiple measurements using different samples of α/β-Cu2ZnSiS4 were performed yielding the same results. The impurity, ZnS, has a melting point around 1700 °C.[13] The DTA residues were analyzed using XRPD. The XRPD pattern for the residue of Cu_2CdSnS_4 matches well to the calculated and shows no additional phases, thus the material melts congruently. It is not possible to definitively determine if α/β-Cu_2ZnSiS_4 melts congruently or incongruently since the sample that went into the DTA tube already contained a small amount of ZnS.

1.7 Optical Diffuse Reflectance UV/VIS/NIR Spectroscopy

A Varian Cary 5000 spectrometer, equipped with a Harrick Praying Mantis diffuse reflectance accessory, was used to collect the optical diffuse reflectance spectra of Cu_2CdSnS_4 and α/β-Cu_2ZnSiS_4 over the ultraviolet, visible, and near infrared (UV/VIS/NIR) spectral regimes. Each sample was ground and a small amount was placed onto a compacted barium sulfate powder that was preloaded into the sample holder with a depth of 3 mm. Barium sulfate (Fisher, 99.92%) was used as a 100% reflectance standard. The measurement was conducted at a scan rate of 600 nm/min. For Cu_2CdSnS_4, the data were treated using the Kubelka-Munk transformation, $\alpha_{KM} / s = (1-R)^2/(2R)$ and the raw reflectance (R) was converted to a relative absorption (α) since the scattering coefficient, *s*, is unknown.[14] The Urbach energy was also obtained by fitting the optical data to the functional form $\alpha = A \cdot \exp[(E-E_g)/E_u]$, where A is a constant, E is the photon energy in eV, E_g is the bandgap energy, and E_u is the Urbach energy.[15] The bandgaps of α/β-Cu_2ZnSiS_4 were roughly estimated by extrapolation of the absorption edge to the baseline as more careful treatment proved difficult since the sample was not a pure material but rather consisted of 59(1)% α-Cu_2ZnSiS_4 , 40(1)% β-Cu_2ZnSiS_4, and 0.3(1)% ZnS.

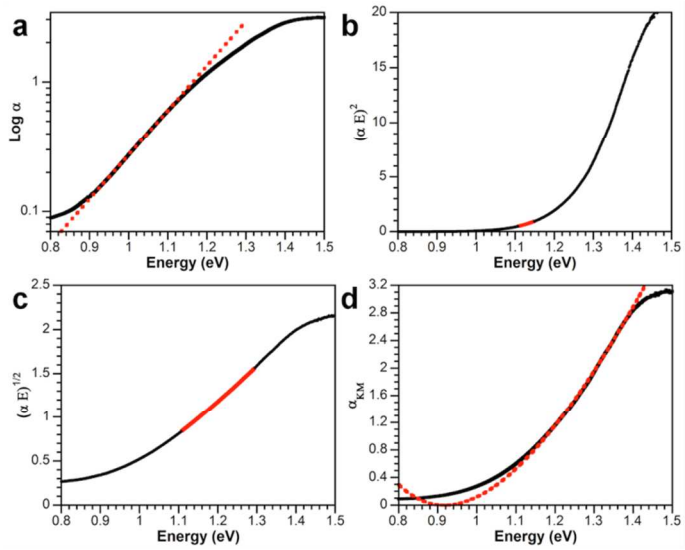

Figure S4. Relative Kubelka-Munk absorption of Cu_2CdSnS_4 derived from the optical diffuse reflectance UV/VIS/NIR spectrum; (a) log of the absorption as a function of energy with an overlaid fit used to determine the Urbach energy (E_u), (b) the square of the absorption as a function of energy (direct bandgap function), where the lighter region shows the linear portion of the curve, (c) the square root of the absorption as a function of energy (indirect bandgap function), where the lighter region shows the linear portion of the curve, and (d) relative absorption as a function of energy where the dotted curve shows the fitting used to estimate the bandgap energy (E_g).

The bandgap, the nature of the gap, and the Urbach tail energy were determined for Cu_2CdSnS_4 via optical diffuse reflectance UV/VIS/NIR spectroscopy data. The Urbach tail arises from impurities and defects within a compound, which essentially smears the top of the valence bands and the bottom of the conduction bands. The Urbach tail can be assigned by finding the linear portion of the data when plotting the logarithm (log) of the absorption as a function of photon energy. The fitting of the slope is the Urbach energy, which was found to be 0.1267(1) eV, Figure S4a. In determining the nature of the bandgap, whether direct (sharp absorption edge) or indirect (gradual onset of absorption edge), the absorption data were fitted to the function for a direct gap semiconductor, $\alpha = A \cdot (E-E_g)^{1/2}/E$ (Figure S4b), and to the function for an indirect semiconductor, $\alpha = A \cdot (E-E_g)^2/E$ (Figure S4c), where A is a constant, E is the photon energy in eV, and E_g is the bandgap energy. The data for Cu_2CdSnS_4 were better fit with the indirect function suggesting that it is an indirect bandgap semiconductor with a bandgap energy of 0.92 eV (Figure S4d). However, we cannot exclude a direct-gap case, in which the optical transition is extrinsically broadened by a significant Urbach tailing effect. Our band structure calculations indicate that Cu_2CdSnS_4 has a direct bandgap as detailed in Section 1.10; however, it should be noted that the calculations are performed for T = 0 K.

The bandgaps of α-Cu_2ZnSiS_4 and β-Cu_2ZnSiS_4 have been previously reported as ~3.0 and ~3.2 eV.[1] It is difficult to assign precise values to the bandgaps of α-Cu_2ZnSiS_4 and β-Cu_2ZnSiS_4 because they are currently prepared as a mixture. Syntheses of pure phases is extremely challenging, due to the very similar ground state energies calculated for the two polymorphs.

1.8 Infrared Spectroscopy

Infrared spectroscopy was carried out using a Thermo Nicolet Nexus 470 FT-IR spectrometer. An ATR attachment with a germanium window was used to collect data from 400 cm^{-1} to 4000 cm^{-1}. The data collection software OMNIC was used to collect 64 scans for $Cu_2CdSnS_4$and α/β-Cu_2ZnSiS_4.

1.9 Nonlinear Optical (NLO) Properties

A summary of all nonlinear optical data is listed in Table S2.

1.9.1 Sample Preparation

Polycrystalline Cu_2CdSnS_4 and a mixture of α/β-Cu_2ZnSiS_4 were sieved into discrete particle size ranges of 0-20 μm, 20-45 μm, 45-63 μm, 63-75 μm, 75-90 μm, and 90-106 μm, in order to assess phase-matching behavior of the samples. In addition, α/β-Cu_2ZnSiS_4 was also sieved into particle size ranges of 106-125 μm and 125-150 μm. Although the samples appear to be air stable, they were placed into fused-silica capillary tubes that were flame-sealed under vacuum to prevent exposure to air and moisture during the measurements. Each tube was loaded into a homemade sample holder that was mounted on a Z-scan translation stage. The microcrystalline $AgGaSe_2$ (MC), a reference material, was prepared by Brant et al.[16] In addition, a comparison between the microcrystalline $AgGaSe_2$ (MC) and an optical-quality single crystal of $AgGaSe_2$ (OQ) found that the $AgGaSe_2$ (MC) sample resulted in lower SHG responses, probably due to a higher defect concentration within the $AgGaSe_2$ (MC) than the $AgGaSe_2$ (OQ).[16] Based on the findings in that work, Li_2CdGeS_4 was compared to the $AgGaSe_2$ (MC) due to the title material probably having a considerable defect concentration.[16] Likewise, the SHG responses of the Cu_2CdSnS_4 and α/β-Cu_2ZnSiS_4 were compared with that of $AgGaSe_2$ (MC). Although α/β-Cu_2ZnSiS_4 is a mixture, we confirmed that the NLO responses measured across various sample spots were reasonably consistent, indicating that the sample is homogeneous.

1.9.2 Second Harmonic Generation (SHG)

Broadband SHG experiments were conducted at room temperature. In order to generate tunable pulses, coherent light of 1064 nm wavelength was first produced using an EKSPLA PL-2250 series diode-pumped Nd:YAG laser with a pulse width of 30 ps and a repetition rate of 50 Hz. The Nd:YAG laser pumped an EKSPLA Harmonics Unit (HU) H400 where the input beam was frequency tripled by a sum frequency generation scheme. The beam then entered an EKSPLA PG403-SH-DFG Optical Parametric Oscillator (OPO) composed of four main parts; a double-pass parametric generator, a single-pass parametric amplifier, a second harmonic generator (SH), and a difference frequency generation (DFG) scheme. The output wavelengths of the OPO used ranged from 1100 to 3300 nm at increments of 200 nm. The corresponding SHG wavelength range is therefore $\lambda_{SHG} = \lambda/2 = 550 - 1650$ nm.

The incident pulse energy was tuned to 15 μJ before being mildly focused onto samples with a spot size of roughly 0.5 mm in diameter by a CaF_2 convex lens. Here we determined the beam spot size in order to i) efficiently generate and properly average the SHG signals from powders of random orientations and to ii) minimize the change in the spot size when the fundamental wavelength, λ, is varied over a broad range (1100–3300 nm); the beam waist w_0 at the focus undergoes a significant λ-dependent variation via $w_0 = (\lambda/\pi)(f/\sigma)$, where f and σ are the focal length and the Gaussian width of the incident beam, respectively.[17] For wavelengths inaccessible with 15 μJ, the NLO counts were properly scaled in accordance with the measured SHG power dependence. The NLO signals from the samples were collected using a reflection geometry by a fiber optic bundle, which was coupled to a selective-grating (1800, 600, and 300 grooves/mm) spectrometer equipped with a charge-coupled device camera (Synapse) as well as an extended InGaAs (Symphony) detector. The overall detection range obtained from the combination of the two detectors was 300-2000 nm. Surface–induced effects as well as SHG signals from other optical components were negligible. Any thermal load on the samples by the laser pulses tuned below the bandgap was negligible due to its slow repetition rate of 50 Hz. The relative SHG signals spectrally resolved in a broad wavelength range were precisely calibrated with the known and measured efficiencies of all optical components.

Figure S5 shows the λ-dependent SHG responses from the title compounds. A dip near λ_{SHG} = 950–1050 nm is common to the samples and the reference, which arises from linear absorption of the fundamental beam by the container (capillary tubes), but this does not affect our estimation of the SHG coefficients.[15] Significantly lower SHG counts for shorter wavelengths arise due to bandgap absorption of SHG light as well as multi-photon absorption (MPA) of the fundamental beam. Such a huge variance in the experimental SHG counts over the range of wavelengths, especially for Cu_2CdSnS_4, clearly emphasizes the importance of the broadband approach for accurate NLO characterization. The size-dependent SHG counts for Cu_2CdSnS_4 and α/β-Cu_2ZnSiS_4 are plotted in Figures S6 and S7, respectively, reconstructed from Figure S5. The results show that both compounds are phase-matchable for longer wavelengths $\lambda_{SHG} \geq 1050$ nm and $\lambda_{SHG} \geq 850$ nm for Cu_2CdSnS_4 and α/β-Cu_2ZnSiS_4, respectively.

In order to estimate $\chi^{(2)}$ of Cu_2CdSnS_4 and α/β-Cu_2ZnSiS_4, the SHG counts must be compared at the static range in which both reference and sample are phase-matchable with minimal absorption effects. Using the Kurtz powder method[18] the static value of $\chi^{(2)}$ for the title compounds can be calculated by comparison with the reference according to:

$$\chi_S^{(2)} = \chi_R^{(2)} \times (I_S^{SHG} / I_R^{SHG})^{1/2}, \qquad \text{(Eq S1)}$$

where I_S^{SHG} and I_R^{SHG} are the measured SHG counts from the sample and the reference, respectively, at the same particle size, *d*. $AgGaSe_2$ is the benchmark mid-IR NLO material with a static SHG coefficient of $\chi^{(2)}$ = 66 pm/V ($\lambda \rightarrow \infty$).[19,20] Our calculation yields a $\chi^{(2)}$ of 62±3 pm/V for Cu_2CdSnS_4 and 15±2 pm/V for α/β-Cu_2ZnSiS_4.

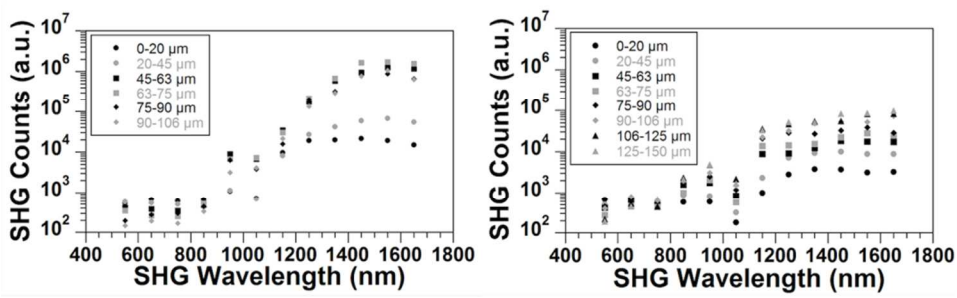

Figure S5. Broadband SHG spectra from Cu_2CdSnS_4 (d=0-106 μm) [left] and α/β-Cu_2ZnSiS_4 (d=0-150 μm) [right].

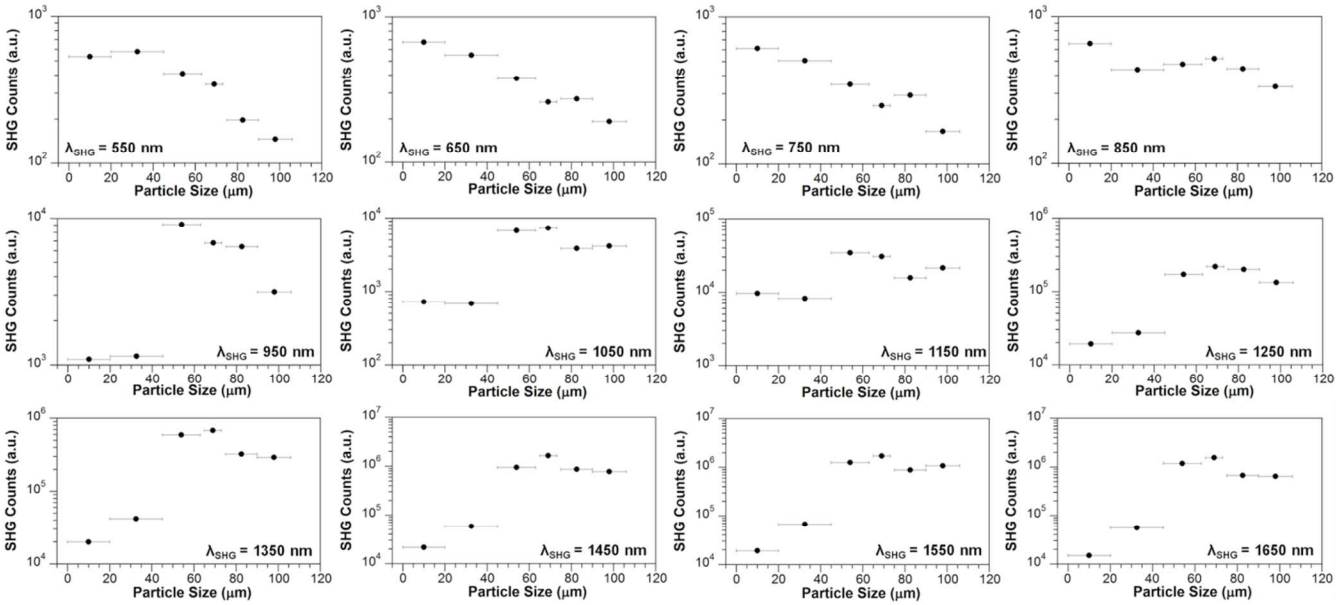

Figure S6. Particle size dependence at 550 nm ≤ λ_{SHG} ≤ 1650 nm of Cu_2CdSnS_4. Cu_2CdSnS_4 exhibits phase-matching behavior for λ_{SHG} ≥ 1050 nm.

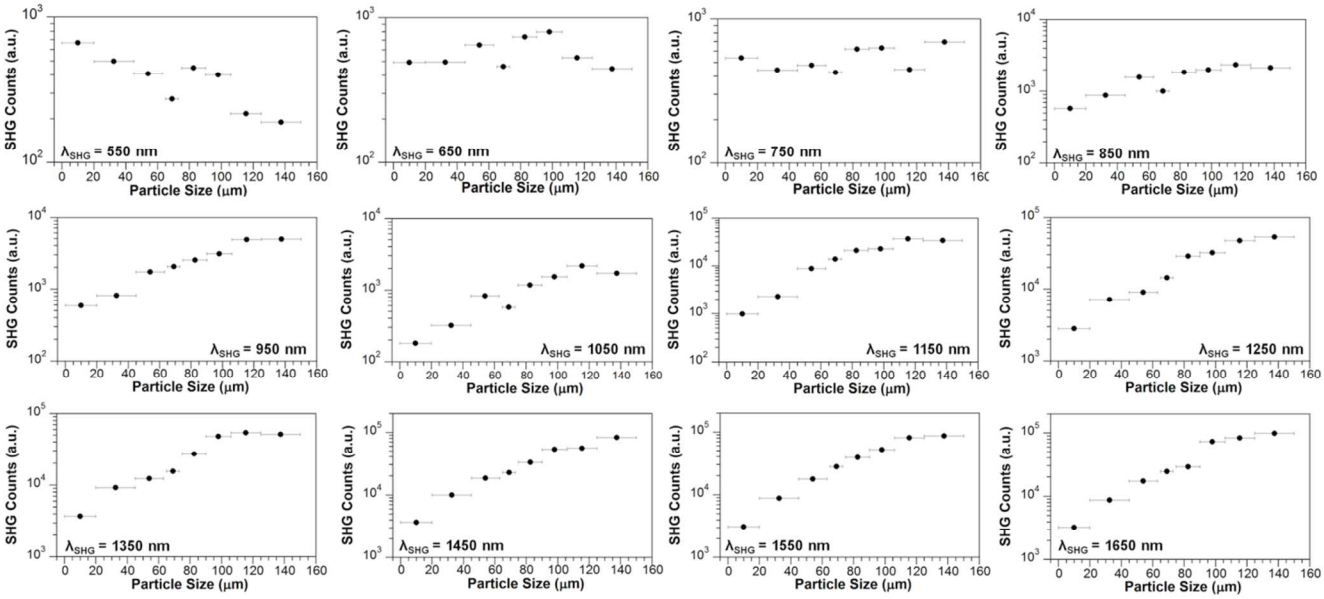

Figure S7. Particle size dependence at 550 nm ≤ λ ≤ 1650 nm of α/β-Cu_2ZnSiS_4. α/β-Cu_2ZnSiS_4 exhibits phase-matching behavior for λ_{SHG} ≥ 850 nm.

1.9.3 Third Harmonic Generation (THG)

Broadband THG experiments were conducted at room temperature with the same excitation source mentioned above for SHG measurements. The output wavelengths of the OPO used in THG experiments ranged from 1300 nm to 3100 nm at increments of 200 nm. The corresponding wavelength ranges for THG is therefore $\lambda_{THG} = \lambda/3$ = 433–1033 nm. The incident pulse energy was tuned to 19 μJ before being focused onto samples with a spot size of ~0.2 mm in diameter by a CaF_2 lens. Collection of THG light was performed in the same manner as mentioned above for SHG experiments. We confirmed that background THG from other optical components as well as frequency tripling by the NLO cascade were negligible. The relative THG signals spectrally resolved in a broad wavelength range were precisely calibrated with the known and measured efficiencies of all optical components (Figure S8). Being a higher-order NLO process, THG is much weaker than SHG; thus, the corresponding data collection time was 60 s. All data were scaled to the 1 s collection time.

In Figure S8 we plot relative THG counts of the samples as a function of λ_{THG} in comparison with those from $AgGaSe_2$ on a semi-log scale at d = 0-20 μm. A dip near λ_{THG} = 700–800 nm arises from linear absorption of the fundamental beam by the container (capillary tubes). Note that a similar effect occurs for the SHG measurements. This effect does not affect our estimation of the THG coefficients. Because of the difference in bandgap energies and relevant linear absorption coefficients, we determined the THG coefficients of the samples at longer wavelengths, i.e., at the static limit ($\lambda \rightarrow \infty$), in which both linear absorption of THG and MPA are minimal.

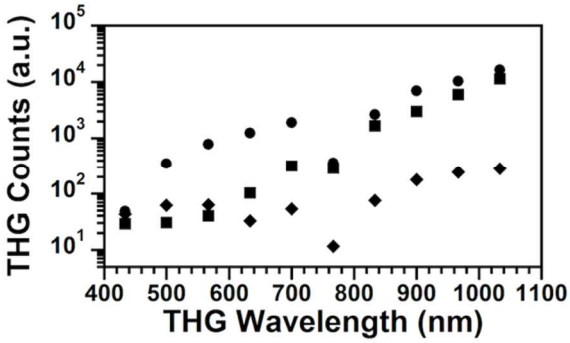

Figure S8. Broadband THG (d = 0-20 μm) spectra from Cu_2CdSnS_4 (▪), α/β-Cu_2ZnSiS_4 (♦), and $AgGaSe_2$ (•), respectively.

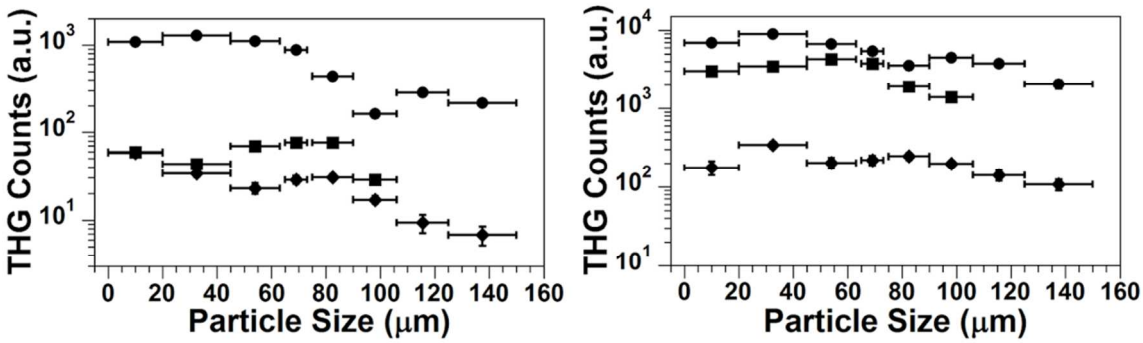

Figure S9. Particle size dependence of THG at λ = 1800 nm (left) and λ = 2700 nm (right) for Cu_2CdSnS_4 (▪), α/β-Cu_2ZnSiS_4 (♦), and $AgGaSe_2$ (•), respectively.

The dots in Figure S9 correspond to the THG particle size dependence of $AgGaSe_2$ at λ = 1800 nm and 2700 nm. A decreasing trend with increasing *d* clearly indicates non-phase-matched THG for *d* > 20 μm. Based on the Kurtz method, the experimental THG coherence length is about d_c = 32.5 ± 12.5 μm, which corresponds to the maximum THG counts. This value together with the reference value of $\chi_R^{(3)} = 1.6 \times 10^5$ pm^2/V^2 was used for estimating $\chi^{(3)}$ values of the samples. The squares in Figure S9 correspond to the case for Cu_2CdSnS_4. The d-dependence at 1800 nm is featureless because the phase-matching factor is washed out by strong bandgap absorption of THG light by the compound.[21] However, at λ = 2700 nm, it indicates a non-phase-matching case, but with a relatively long THG coherence length of d_c = 54 ± 9 μm. Note that the THG efficiency of Cu_2CdSnS_4 is significantly enhanced at 2700 nm compared to that at 1800 nm. The THG particle size dependence for α/β-Cu_2ZnSiS_4 at these two input wavelengths also indicates a non-phase-matching case as plotted by the diamonds in Figure S9. Note that the THG coherence length increases from d_c = 10 ± 10 μm at 1800 nm to d_c = 32.5 ± 12.5 μm at 2700 nm. This trend is typical due to a reduced phase mismatch at longer wavelengths. We found that all samples and the reference are non-phase-matchable within our experimental range, although we only show the results for two incident wavelengths here.

The absolute $\chi^{(3)}$ value of the sample can be estimated by comparing with the reference using:

$$\chi_S^{(3)} = \chi_R^{(3)} \times (I_S^{THG} / I_R^{THG})^{1/2} \times (d_{c,R} / d_{c,S}), \quad \text{(Eq S2)}$$

where I_S^{THG} and I_R^{THG} are the measured THG counts from the sample and the reference at the same particle size and $d_{c,S}$ and $d_{c,R}$ are the corresponding coherence lengths determined from the data in Figure S9. Using $\chi_R^{(3)} = 1.6 \times 10^5$ pm²/V², our calculation yields a $\chi^{(3)}$ for Cu_2CdSnS_4 of ~(0.8±0.2) $\times 10^5$ pm²/V² at 3100 nm, but this is very likely underestimated due to the bandgap absorption issue. The estimated $\chi^{(3)}$ for α/β-Cu_2ZnSiS_4 is ~(0.21±0.06) $\times 10^5$ pm²/V². This relatively low value is predicted due to its large bandgap.[22]

1.9.4 Laser-Damage Threshold (LDT)

In order to estimate damage thresholds of the compounds, SHG measurements were carried out on the samples with d= 90 – 106 μm as a function of laser intensity in the range of 0.3 – 17 GW/cm² using a typical Nd:YAG transition line of 1064 nm with a temporal pulse width of 30 ps. The damage threshold of a material significantly depends on the pulse width and here is a picosecond case. All experiments were conducted at room temperature.

The spectrally integrated SHG counts from Cu_2CdSnS_4 as a function of input intensity are shown in Figure S10. The dotted line represents the maximum SHG case in which fundamental depletion is absent, i.e. $I_{SHG} = aI^2$, where I_{SHG} and I are the SHG and fundamental intensities with *a* being a proportionality constant that incorporates $|\chi^{(2)}|^2$. Although the compound has a high $\chi^{(2)}$ and $\chi^{(3)}$, it undergoes serious damage upon laser illumination due to efficient one-photon absorption (1PA) at 1064 nm (Figure S10). The LDT seems to be below 1 GW/cm². A similar experiment was conducted with an incident wavelength of 1300 nm, due to strong absorption at 1064 nm. The LDT of Cu_2CdSnS_4 was estimated as 0.2 GW/cm² at 1300 nm (Figure 3). We estimated the corresponding 2PA coefficient (~120 cm/GW) by fitting the measured SHG power dependence using a modified fundamental intensity by 2PA, I_{2PA};

$$I_{SHG} = aI_{2PA}^2 \text{ with } I_{2PA} = I/[1 + I\beta d] \quad \text{(Eq S3)}$$

Figure 3 also illustrates the case for α/β-Cu_2ZnSiS_4. Considering the bandgap of the compound, we concluded that it undergoes three-photon absorption (3PA) of the fundamental beam I > 2 GW/cm², as evidenced by the deviation from the dotted line (maximum SHG). We estimated the corresponding 3PA coefficient γ by fitting the measured SHG power dependence using a modified fundamental intensity by 3PA, I_{3PA};

$$I_{SHG} = aI_{3PA}^2 \text{ with } I_{3PA} = I/[1+ 2\gamma dI^2]^{1/2}, \text{ (Eq S4)}$$

where *d* = 90-106 μm is roughly the particle size for our reflection-based collection geometry and the constant, *a,* was carefully determined by fitting the low-intensity regime where 3PA is absent. The solid trace on top of the data points in Figure 3 is a fit using Equation S4, yielding γ = 1.22 cm³/GW². This value is higher than typical 3PA coefficients of inorganic materials having similar bandgaps.[23,24] This may arise from optical damage induced by significant 3PA.

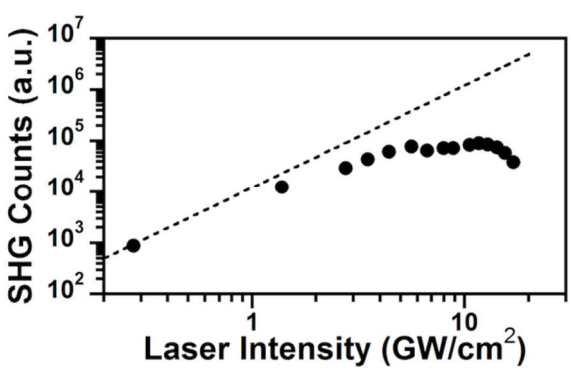

Figure S10. SHG power dependence of Cu_2CdSnS_4 at 1064 nm.

Table S2. Comparison of SHG, THG, LDT, and phase matchability for Cu_2CdSnS_4, α/β-Cu_2ZnSiS_4, and $AgGaSe_2$.

	SHG			THG
Compound	$\chi^{(2)}$ (pm/V)	Phase matching region (nm)	LDT (GW/cm²)	$\chi^{(3)}$ (pm²/V²)

Cu_2CdSnS_4	62±3	$\lambda_{SHG} \geq 1050$	0.2	$(8.0\pm2.0) \times 10^4$
α/β-Cu_2ZnSiS_4	15±2	$\lambda_{SHG} \geq 850$	2.0	$(2.1\pm0.6) \times 10^4$
$AgGaSe_2$	66	$\lambda_{SHG} \geq 1550$	0.2	1.6×10^5

1.10 Electronic Structure

The electronic structures of Cu_2CdSnS_4, α-Cu_2ZnSiS_4 and β-Cu_2ZnSiS_4 were calculated. Although calculations on Cu_2CdSnS_4 have previously been reported using VASP and the projector augmented wave (PAW) method with the Perdew, Burke, and Ernzerhof (PBE) exchange correlation approximation and the Heyd-Scuseria-Ernzerhof (HSE) hybrid functional,[25] our calculations expand upon those previously reported, particularly the partial density of states (PDOS) contributions. The electronic structures of α-Cu_2ZnSiS_4 and β-Cu_2ZnSiS_4 have been previously calculated.1 Here CASTEP was used to determine the electronic band structures of α-Cu_2ZnSiS_4 and β-Cu_2ZnSiS_4; the bandgap energies were found to be closer to the experimental bandgap energies than those previously calculated. Additionally, an exchange potential, the modified Becke-Johnson (mBJ) potential for improving bandgap determination in semiconductors, was employed within the WIEN2k software.[26] All of the calculated bandgap values are markedly underestimated which is a well-known problem of DFT calculations using the Perdew-Burke-Ernzerhof generalized gradient approximation (PBE-GGA).[27]

1.10.1 CASTEP

The refined crystal structures of Cu_2CdSnS_4, α-Cu_2ZnSiS_4, and β-Cu_2ZnSiS_4 were used for the electronic structure calculations carried out using the total-energy code of CASTEP to determine the electronic band structure as well as density of states (DOS) (Figure S11). In addition, quantitative bond analysis was performed.[28,29] In CASTEP, the total energy is calculated using the plane-wave pseudopotential method within density functional theory (DFT). The PBE-GGA was used to treat the exchange and correlation effects.[30] Using this method, the interactions between the ionic cores and the electrons are described by norm-conserving pseudopotentials.[31] The number of plane-waves included in the basis set was determined by a cutoff energy of 600 eV for all compounds. The numerical integration of the Brillouin zone was performed using a 5×5×6, 3×4×4 and 4×4×3 Monkhorst-Pack k-point sampling for Cu_2CdSnS_4, α-Cu_2ZnSiS_4 and β-Cu_2ZnSiS_4, respectively. The self-consistent field (SCF) tolerance was set to 1 x 10^{-6} eV/atom for the convergence criteria and 100 cycles were performed. The interpolation integration method was used for the DOS analysis. For all compounds, a Mulliken bond population analysis within the CASTEP code was used to calculate the bond orders (Table S3).[32,33] Direct bandgaps of 0.69 eV and 1.69 eV at the Γ-point were calculated for Cu_2CdSnS_4 and α-Cu_2ZnSiS_4. An indirect band gap of 2.23 eV was calculated for β-Cu_2ZnSiS_4.

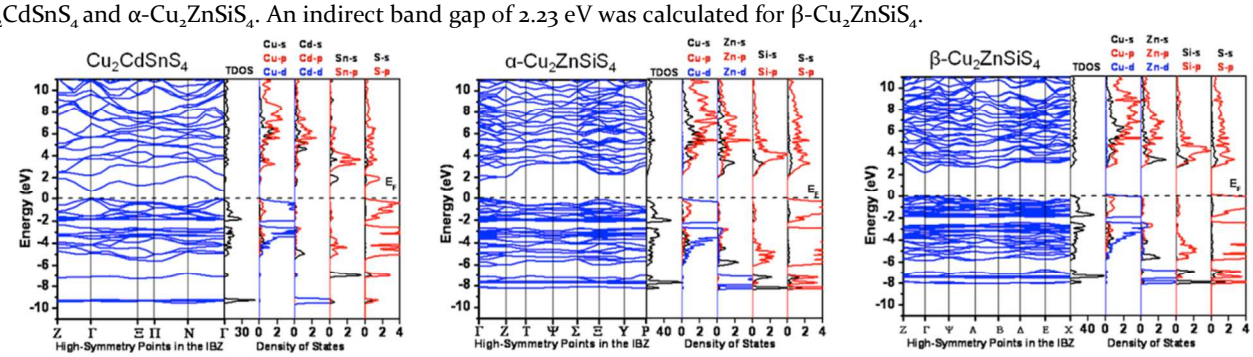

Figure S11. Calculated electronic band structure shown on the left of each plot and TDOS and PDOS shown on the right side of each plot using CASTEP. DOS and PDOS are shown in electrons/eV. The dotted line denotes the Fermi level (E_F).

Table S3. The Mulliken bond population data.

	Bonds				
Compound	Cu-S Avg. Bond Order	Zn-S Avg. Bond Order	Cd-S Avg. Bond Order	Si-S Avg. Bond Order	Sn-S Avg. Bond Order
Cu_2CdSnS_4	0.37	NA	0.32	NA	0.49
α-Cu_2ZnSiS_4	0.36	0.42	NA	0.70	NA
β-Cu_2ZnSiS_4	0.37	0.42	NA	0.69	NA

The total DOS (TDOS) and PDOS for Cu_2CdSnS_4 are shown in Figure S11. The valence band region from -10 to -7.5 eV chiefly originates from Cd-4d orbitals along with minor contributions from the S-3*s*, S-3*p*, Sn-5*s*, and Sn-5*p* orbitals, whereas the states in the region from -7.5 to -6.0 eV mainly arise from S-3*s*, S-3*p*, Sn-5*s*, and Sn-5*p* orbitals. Approaching the top of the valence band from -6.0 to -2.5 eV, the states are largely due to S-3*p*, Sn-5*p*, Cu-4*d* orbitals with lesser influence from Sn-5*s*, Cd-5*s*, Cu-4*s*, and Cu-3*p* orbitals. The states in the highest energy valence band region closest to the Fermi level (E_F), -2.5 to 0 eV, primarily arise from the S-3*p*, Sn-5*p*, and Cu-4*d* orbitals, with slight contributions from S-3*s*, Sn-5*s*, Cd-4*p*, Cu-5*s* and Cu-3*p* orbitals. The minimum states in the conduction band 0.69 to 2.5 eV are mainly attributed to S-3*p* and Sn-5*s* orbitals. Higher in the conduction band from 2.5 to 5 eV, the states are principally from the Sn-5*s* obritals along with donations from the S-3*p*, Sn-5*s*, and Cu-3*p* orbitals and very small contributions from the S-3*s*, Cd-5*s*, Cd-4*p*, and Cu-4*s*. From 5.0 to 10 eV the states evolve largely from the

Sn-5*p*, Sn-5*s*, S-3*p*, and Cu-3*p* orbitals, with additional contributions from S-3*s*, Cd-5*s*, and Cd-4*p* orbitals. The Cd orbitals in Cu_2CdSnS_4 and the Zn orbitals in α-Cu_2ZnSiS_4 have an extremely small contribution to the E_F.

1.10.2 WIEN2K

The band structure and DOS of Cu_2CdSnS_4, α-Cu_2ZnSiS_4 and β-Cu_2ZnSiS_4 were also carried out using the WIEN2k package, which utilizes the full-potential linearized augmented plane-wave method (FLAPW) within DFT for solving the Kohn-Sham equations for total energy (Figure S12). [34-36] The PBE-GGA was used to treat the exchange and correlation effects; in addition the mBJ exchange potential was used to achieve greater accuracy of the bandgap energies in semiconductors.[30] In these calculations, the muffin tin radii (RMT) of Cu, Zn, Si, and S were set to 2.39, 2.40, 1.85, and 1.96 bohr, respectively. With respect to Cu_2CdSnS_4, the RMT values were set to 2.39, 2.50, 2.49, and 1.96 bohr, respectively for Cu, Cd, Sn, and S. SCF calculations converged when the energy difference between successive iterations fell below 0.1 mRy/unit cell. Additionally, a total of 3,000 k-points were used in the full Brillouin zone for each compound, which corresponded to 336, 630, and 240 k-points in the irreducible Brillouin zone (iBZ) for the Cu_2CdSnS_4, α-Cu_2ZnSiS_4 and β-Cu_2ZnSiS_4 structures, respectively.

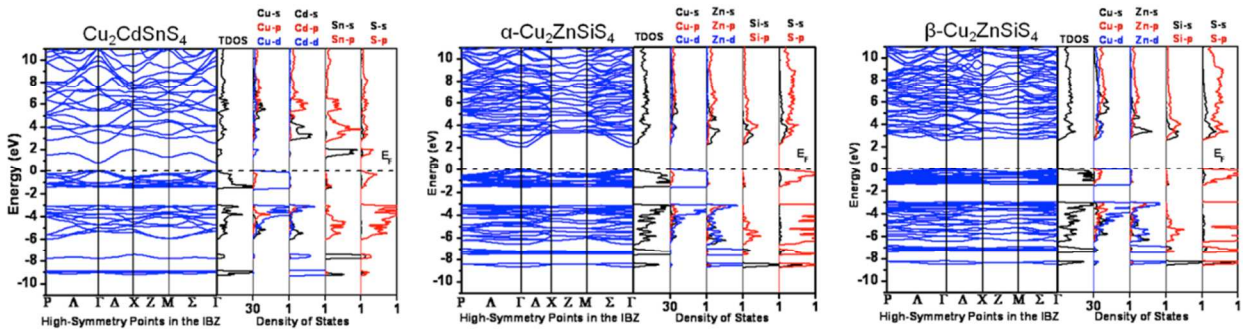

Figure S12. Calculated electronic band structure shown on the left of each plot and TDOS and PDOS shown on the right side of each plot using WIEN2k. DOS and PDOS are shown in states/eV. The dotted line denotes the Fermi level (E_F).

The bandgap for α-Cu_2ZnSiS_4 was previously calculated to be 1.3 eV using WIEN2k. Here, the electronic structures of α-Cu_2ZnSiS_4 and β-Cu_2ZnSiS_4 were recalculated using the WIEN2k software but with the addition of the mBJ potential, which resulted in better agreement between calculated and experimental bandgap values.[26] Using this potential, direct bandgaps of 0.79 eV, 2.05, and 2.57 eV at the Γ-point were calculated for Cu_2CdSnS_4, α-Cu_2ZnSiS_4, and β-Cu_2ZnSiS_4, respectively. Inclusion of the mBJ potential, however, barely alters the TDOS and PDOS for α-Cu_2ZnSiS_4 and β-Cu_2ZnSiS_4. Additionally, when the PDOS was calculated using the mBJ potential in the WIEN2k software, the PDOS contributions are very similar to the description already described in Rosmus et al.1 The discrepancy in the nature of the band gap for β-Cu_2ZnSiS_4 (direct versus indirect) results from using two software packages that employ different methods. However, it should be noted that the band structures obtained using both methods indicate a number of low energy transitions for the compound that are closely spaced in energy.

Table S4. Comparison of calculated bandgap energies using WIEN2k (PBE-GGA)1, WIEN2k (PBE-GGA+mBJ), and CASTEP (PBE-GGA).

Compound	WIEN2k PBE-GGA Bandgap energy (eV)	WIEN2k PBE-GGA+mBJ Bandgap energy (eV)	CASTEP PBE-GGA Bandgap energy (eV)
Cu_2CdSnS_4		0.79 direct	0.69 direct
α-Cu_2ZnSiS_4	1.3 direct	2.05 direct	1.69 direct
β-Cu_2ZnSiS_4	1.7 direct	2.57 direct	2.23 indirect

References

(1) Rosmus, K. A.; Brunetta, C. D.; Srnec, M. N.; Karuppannan, B.; Aitken, J. A. *Z. Anorg. Allg. Chem.* **2012**, *638*, 2578-2584.
(2) Bruker **1998** SMART and SAINT, Bruker AXS Inc., Madison, Wisconsin, USA.
(3) Sheldrick, G. M. **2002** SADABS. University of Göttingen, Germany.
(4) Wang, J.; Toby, B. H.; Lee, P. L.; Ribaud, L.; Antao, S.; Kurtz, C.; Ramanathan, M.; Von Dreele, R. B.; Beno, M. A. *Rev. Sci. Instrum*. **2008**, *79*, 085105-085111.
(5) Lee, P. L.; Shu, D.; Ramanathan, M.; Preissner, C.; Wang, J.; Beno, M. A.; Von Dreele, R. B.; Ribaud, L.; Kurtz, C.; Antao, S. M.; Jiao, X.; Toby, B. H. *J. Synchrotron Radiat*. **2008**, *15*, 427-432.
(6) Toby, B. H. *J. Appl. Crystallogr.* **2001**, *34*, 210–213.
(7) Dalesio, L. R.; Hill, J. O.; Kraimer, M.; Lewis, S.; Murray, D.; Hunt, S.; Watson, W.; Clausen, M.; Dalesio, J. *Nucl. Instrum. Methods Phys. Res., Sect. A.* **1994**, *352*, 179-184.
(8) Larson, A. C.; Von Dreele, R. B. Los Alamos National Laboratory Report, LAUR 86-748 **2004**.
(9) Abramowitz, M.; Stegun, I. A. (Eds.), *Handbook of Mathematical Functions*; Dover Publications: Dover, NY, 1965. (Ch. 22).
(10) Rosmus, K. A.; Aitken, J. A. *Acta Cryst. E.* **2011**, *67*, i28.
(11) Jumpertz, E. A. *Z Elektrochemie* **1955**, *59*, 419-425.
(12) Matsushita, H.; Katsui, A. *J. Phys. Chem. Sol.* **2005**, *66*, 1933-1936.
(13) *CRC Handbook of Chemistry and Physics, 84th Ed.*; Lide, D.R., Ed.; CRC Press: Boca Raton, FL, 2003; Section 4, pg. 96.
(14) Kubelka, P.; Monk, F. *Z. Technol. Phys.* **1931**, *12* 593–601.
(15) Urbach, F. *Phys. Rev.* **1953**, *92*, 1324.
(16) Brant, J. A.; Clark, D. J.; Kim, Y. S.; Jang, J. I.; Zhang, J.-H.; Aitken, J. A. *Chem. Mater.* **2014**, *26*, 3045-3048.
(17) Jang, J. I.; Park, S.; Clark, D. J.; Saouma, F. O.; Lombardo, D.; Harrison, C. M.; Shim, B. *J. Opt. Soc. Am*. **2013**, *30*, 2292-2297.
(18) Kurtz, S. K.; Perry, T. T. *J. Appl. Phys.* **1968,** *39*, 3798-3813.
(19) Nikogosyan, D. N. *Nonlinear optical crystals: A complete survey, 1st edition*; Springer: New York, 2005.
(20) Bhar, G. C. *Jpn. J. Appl. Phys. Part I, Supplement* **1993**, *32*, 653-659.
(21) Shen, Y. R. *Principles of nonlinear optics*; John Wiley and Sons: New Jersey, 1984.
(22) Boyd, R. W. *Nonlinear Optics, 3rd edition;* Academic Press, San Diego, 2008.
(23) Brandi, H. S.; de Araujo, C. B. *J. Phys. C* **1983**, *16*, 5929–5936.
(24) He, J.; Qu, Y.; Li, H.; J. Mi, J.; Ji, W. *Opt. Express* **2005**, *13*, 9235–9247.
(25) Xiao, Z.-Y.; Li, Y.-F.; Yao, B.; Deng, R.; Ding, Z.-H.; Wu, T.; Yang, G.; Li, C.-R.; Dong, Z.-H.; Liu, L.; Zhang, L.-G.; Zhao, H.-F. *J. Appl. Phys.* **2013**, *114*, 183506.
(26) Koller, D.; Tran, F.; Blaha, P. *Phys. Rev. B.* **2011**, *83*, 195134.
(27) Lee, J. G. Computational Materials Science: An Introduction, 1st ed., CRC Press , Florida **2012**, p. 135-141.
(28) Segall, M. D.; Lindan, P. J. D.; Probert, M. J.; Pickard, C. J.; Hasnip, P. J.; Clark, J. S.; Payne, M. C. *J. Phys.: Condens. Matter* **2002**, *14*, 2717-2744.
(29) Milman, V.; Winkler, B.; White, J. A.; Pickard, C. J.; Payne, M. C.; Akhmatskaya, E. V.; Nobes, R. H. *Int. J. Quantum Chem*. **2000**, *17*, *895*-910.
(30) Perdew, J. P.; Burke, S.; Ernzerhof, M. *Phys. Rev. Let*. **1996**, 77, 3865-3868.
(31) Lin, J. S.; Qteish, A.; Payne, M. C.; Heine, V. *Phys. Rev. B* **1993**, *47*, 4174-4180.
(32) Mulliken, R. S. *J. Chem. Phys.* **1955**, *23*, 1833–1840.
(33) Segall, M. D.; Shah, R.; Pickard, C. J.; Payne, M. C. *Phys. Rev. B* **1996**, *54*, 16317-16320.
(34) Blaha, P.; Schwarz, K.; Madsen, G. K. H.; Kvasnicka, D.; Luitz, J. Vienna University of Technology, Austria, **2011**.
(35) Schwarz, K.; Blaha, P. *Comput. Mater. Sci.* **2003**, *28*, 259–273.
(36) Kohn, W.; Sham, L. *Phys. Rev. A* **1965,** *140*, 1133-1138.